THE JOURNAL OF PHYSICAL CHEMISTRY B
A JOURNAL OF THE AMERICAN CHEMICAL SOCIETY

pubs.acs.org/JPCB
Article

Assessing Fluoroacetate Defluorination Potential across Diverse Enzymes Using Quantum Chemistry

Ayesh Madushanka, Chamindu Jayathilake, Nipuni Prematilaka, Eustace Fernando,* and Elfi Kraka*

Cite This: J. Phys. Chem. B 2026, 130, 7349−7363
Read Online

ACCESS | Metrics & More | Article Recommendations | Supporting Information

ABSTRACT: Fluorinated organic compounds are persistent environmental contaminants due to the exceptional strength of the carbon−fluorine bond, rendering biological defluorination both rare and mechanistically challenging. Fluoroacetate dehalogenase from *Rhodopseudomonas palustris* (strain ATCC BAA-98/CGA009; RPA1163) is one of the few experimentally characterized enzymes capable of C−F bond cleavage and provides a model system for understanding enzymatic defluorination. Here, we establish a mechanistically informed, multiscale computational framework to identify and characterize fluoroacetate dehalogenase-like enzymes across diverse bacterial lineages. Starting from sequence-based screening, 184 candidate proteins spanning nine bacterial classes were identified, from which 12 representative systems were selected for detailed analysis. High-confidence structural models generated with AlphaFold2 were subjected to microsecond-scale molecular dynamics simulations to assess conformational stability and active-site organization. To probe catalytic determinants at the electronic-structure level, QM/MM calculations combined with local vibrational mode analysis were employed to quantify hydrogen-bonding interactions within the binding pocket and relate them to catalytic competence. Across all systems, we observe a conserved network of active-site interactions that stabilizes substrate binding and is consistent with experimentally characterized defluorinases. Notably, specific homologues exhibit hydrogen-bonding patterns and active-site geometries closely matching the reference enzyme, suggesting a previously unrecognized distribution of defluorinase activity across multiple bacterial classes. These results identify key interaction motifs that differentiate likely active enzymes from inactive homologues and provide a mechanistic basis for C−F bond activation in this enzyme family. Overall, this work demonstrates how integrated multiscale simulations can be used to connect sequence diversity to catalytic function in challenging enzymatic reactions. The identified candidates and mechanistic descriptors provide a foundation for the discovery, engineering, and experimental characterization of defluorinase enzymes, opening opportunities for the bioremediation of fluorinated pollutants, including PFAS compounds.

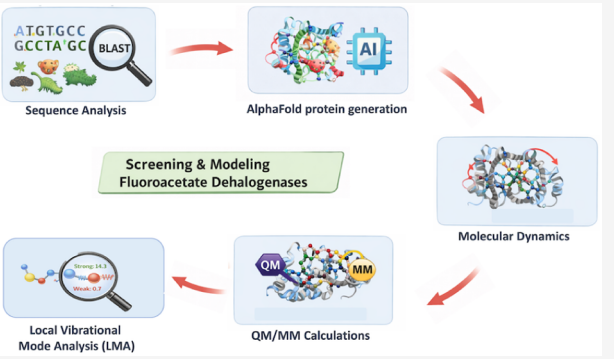

INTRODUCTION

Organofluorine compounds are predominantly synthetic, as naturally occurring C−F-containing molecules are rare.[1] The carbon−fluorine bond is the strongest carbon−halogen bond, with bond dissociation energies reaching approximately 485 kJ mol^{-1}, contributing to the exceptional chemical stability of fluorinated compounds.[2] This exceptional stability arises from fluorine's extremely high electronegativity, which induces strong bond polarization and significant ionic character. In addition, the low polarizability of fluorine and the limited accessibility of its valence electrons further reduce the reactivity of the C−F bond, rendering it highly resistant to chemical transformation.[3,4] Fluorinated organic compounds exhibit distinctive physicochemical properties, including high chemical inertness and pronounced amphiphobicity, characterized by both hydrophobic and lipophobic behavior.[5,6] Per- and polyfluoroalkyl substances (PFAS) represent an important subclass of these materials and have emerged as significant environmental contaminants due to their extraordinary chemical stability, persistence in natural ecosystems, and strong resistance to degradation, with an estimated half-life of over 47 years in water.[7] Owing to these properties, PFAS have been extensively employed in a wide range of industrial and consumer applications, such as textiles, thermal insulation, nonstick cookware, adhesives, and food-contact packaging.[8,9] Consequently, per- and polyfluoroalkyl substances (PFAS) and their precursors (e.g., fluorotelomer alcohols, carboxylic acids, and sulfonates) have become pervasive environmental contaminants. Mounting evidence of their adverse health impacts has led to increasingly stringent regulatory con-

Received: May 5, 2026
Revised: June 17, 2026
Accepted: July 2, 2026
Published: July 8, 2026

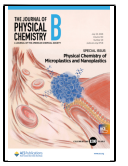

https://doi.org/10.1021/acs.jpcb.6c02887
J. Phys. Chem. B 2026, 130, 7349−7363

trols.[10,11] In response, biodegradation-based remediation strategies have gained significant attention.[12] However, the exceptional stability of the C−F bond and the highly fluorinated molecular environment severely limit enzymatic accessibility, rendering natural defluorinating enzymes exceedingly rare. The scarcity of naturally occurring organofluorine compounds further contributes to this limitation. Representative examples include monofluoroacetic acid, ω-fluorooleic acid, fluorothreonine, and 5-fluorouracil.[13] The biosynthesis of many such compounds is mediated by fluorinase enzymes, which catalyze the formation of C−F bonds.[14] In contrast, the cleavage of these exceptionally strong bonds is carried out by defluorinase enzymes. However, current understanding of the diversity, catalytic mechanisms, and substrate scope of defluorinases remains highly limited.[15] Defluorinases are generally classified within the broader family of dehalogenases, which catalyze the cleavage of carbon−halogen (C−X) bonds. While a wide range of organohalogen compounds, particularly chlorinated substrates, are readily degraded by diverse dehalogenases, enzymatic defluorination remains comparatively rare.[16] Although enzymatic defluorination remains comparatively rare, several biological and bioinspired systems have been reported to promote C−F bond cleavage under specific catalytic conditions. Examples include cytochrome P450-mediated oxidative defluorination and bioactivation of sunitinib, P450-catalyzed aromatic defluorination, heme dehaloperoxidase/peroxidase-mediated defluorination of fluorophenols, and engineered metalloenzyme or P450 systems capable of C−F bond activation.[16−24] Defluorination is proposed to occur via two principal mechanisms: (i) direct cleavage of the highly stable C−F bond, and (ii) indirect removal of fluorine following metabolic activation of the substrate. Among naturally occurring defluorinating enzymes, fluoroacetate dehalogenase (EC 3.8.1.3) represents a well-characterized system for direct hydrolytic cleavage of the aliphatic C−F bond.[25] This enzyme has been identified in a limited number of bacterial species, including *Burkholderia*, *Pseudomonas*, and *Moraxella*, where it catalyzes the hydrolytic defluorination of fluoroacetate.[26]

$$\text{Fluoroacetate} + H_2O \rightleftharpoons \text{glycolate} + \text{fluoride} \quad (1)$$

Two well-resolved and widely studied crystal structures of fluoroacetate dehalogenase are available in the Protein Data Bank (PDB), corresponding to *Rhodopseudomonas palustris*[16] and *Burkholderia* sp. strain FA1.[27] Consequently, our current understanding of the mechanism of fluoroacetate dehalogenase, including substrate binding, stabilization, and catalysis, primarily originates from the two structurally resolved enzymes from *Rhodopseudomonas palustris*[16] and *Burkholderia* sp. strain FA1.[28] These structures offer essential insights into catalytic residues, enzyme kinetics, and the associated reaction mechanisms. *Rhodopseudomonas palustris* (strain ATCC BAA-98/CGA009), belonging to class Alphaproteobacteria with the UniProt accession number Q6NAM1 (RPA1163) is uniquely valuable due to its extraordinary metabolic flexibility,[29] genetic tractability,[30] and well-established mechanistic foundation,[31,32] making it an ideal reference model for studying and benchmarking other bacterial species with potential for enzymatic C−F bond cleavage. Bacterial species known to possess fluoroacetate dehalogenase enzymes are primarily distributed across four classes, including Alphaproteobacteria,[16] Betaproteobacteria,[33] Gammaproteobacteria[27] and Synergistia.[34] Considering that other classes may possess fluoroacetate dehalogenase enzymes, computational approaches offer a rational and resource-efficient first step, enabling targeted experimental investigations rather than broad, costly screening.

However, several significant challenges currently limit large-scale computational studies for screening proteins with similar activity. First, the number of experimentally resolved protein structures available as reliable starting points remains limited.[35] Second, AI-generated protein structures require validation through extensive molecular dynamics simulations,[36] which are computationally demanding. Third, high-level quantum mechanical methods such as Hartree−Fock (HF) and density functional theory (DFT) are restricted to relatively small systems[37] and are not directly applicable to protein-scale systems comprising hundreds to thousands of atoms.[38] Fourth, semiempirical and hybrid Quantum Mechanics/Molecular Mechanics (QM/MM) approaches, while more scalable, remain computationally expensive and require careful system preparation,[39] making them less suitable for high-throughput screening. Finally, conventional geometric descriptors such as bond lengths are not sufficiently accurate as quantitative measures of protein−ligand hydrogen bond strengths.[40]

Large-scale computational analysis of enzymes with conserved activity across diverse species was beyond reach until recently. This limitation stemmed primarily from the lack of reliable methods to predict accurate three-dimensional protein structures directly from amino acid sequences. Recent advances in AI-based protein structure prediction tools, such as AlphaFold2 and Rosetta,[41] have fundamentally transformed this landscape, making large-scale comparative enzymatic studies possible. Although these methods have demonstrated remarkable success and are often reported to approach experimental accuracy, they still suffer from several inherent limitations. These include inaccuracies in modeling flexible loops, active-site conformational variability, cofactor and ligand binding states, metal coordination environments, and protonation states.[36,42] Consequently, predicted structures often require further validation and refinement before being used in advanced computational studies.[43] Therefore, a robust and systematic computational protocol is essential for accurately studying enzymes with conserved activity across a large number of species. Here, we introduce an integrated computational framework that combines Basic Local Alignment Search Tool (BLAST)-based[44] sequence analysis to identify homologous enzymes, protein structure prediction using AlphaFold2 (AF2), and microsecond-scale molecular dynamics (MD) simulations to validate and refine structural stability. This is followed by hybrid QM/MM calculations to achieve high-accuracy descriptions of protein−ligand (PL) interactions, and local vibrational mode analysis (LMA) to quantify intrinsic protein−ligand bond strengths. Together, this protocol enables reliable identification, classification, and comparison of enzymatic potential across species.

The major objectives of the present study were: (i) to explore other species with potential defluorination activity using Q6NAM1 (RPA1163) as a reference; (ii) to investigate the protein−ligand interactions of the defluorinase enzymes produced by those organisms using quantum chemical and vibrational analyses; (iii) to compare the protein−ligand interaction strengths of these selected species with those of RPA1163; (iv) and to demonstrate a novel computational protocol that enables reliable identification, classification, and

https://doi.org/10.1021/acs.jpcb.6c02887
J. Phys. Chem. B 2026, 130, 7349−7363

Table 1. Reference Protein and Selected Proteins from BLAST Analysis with Taxonomic Classification and Sequence Similarity Values Given by the BLAST Analysis to Q6NAM1 (RPA1163)[a]

Index	UniProt Accession	Species Name	Kingdom	Phylum	Class	Similarity (%)
1	Q6NAM1 (**Reference**)	*Rhodopseudomonas palustris* (strain ATCC BAA-98/CGA009)	Pseudomonadati	Pseudomonadata	Alphaproteobacteria	Reference
2	A0A4U5JW23 (**P1**)	*Luteimonas gilva*	Pseudomonadati	Pseudomonadata	Gammaproteobacteria	50.3
3	A0A4Z0BVY8 (**P2**)	*Ramlibacter rhizophilus*	Pseudomonadati	Pseudomonadata	Betaproteobacteria	65.4
4	A0A8J7A8L8 (**P3**)	*Vasconcelosia minhoensis*	Bacillati	Cyanobacteriota	Cyanophyceae	51.0
5	A0A9×3N3I3 (**P4**)	*Solirubrobacter ginsenosidimutans*	Bacillati	Actinomycetota	Thermoleophilia	50.5
6	A0A172ZIM2 (**P5**)	*Paenibacillus bovis*	Bacillati	Bacillota	Bacilli	50.9
7	A0A387B7I1 (**P6**)	*Protaetiibacter intestinalis*	Bacillati	Actinomycetota	Actinomycetes	52.0
8	A0A447CYM1 (**P7**)	*Rhodoplanes serenus*	Pseudomonadati	Pseudomonadata	Alphaproteobacteria	59.1
9	Q2IYY8 (**P8**)	*Rhodopseudomonas palustris* (strain HaA2)	Pseudomonadati	Pseudomonadata	Alphaproteobacteria	82.7
10	A0A1B9Z5E1 (**P9**)	*Bradyrhizobium* sp. LMTR 3	Bacteria	Pseudomonadata	Alphaproteobacteria	71.3
11	A0A2W2AYK9 (**P10**)	*Aestuariivirga litoralis*	Pseudomonadati	Pseudomonadata	Alphaproteobacteria	50.3
12	A0A7 V8CW33 (**P11**)	*Chloroflexia bacterium* SDU3−3	Bacillati	Chloroflexota	Chloroflexia	50.9
13	A0A927B728 (**P12**)	*Spirosoma validum*	Pseudomonadati	Bacteroidota	Bacteroidota	51.8

[a]P1−P12 with the reference are involved in QM/MM and LMA calculations.

comparison of enzymes with conserved activity across a large number of species.

METHODOLOGY

Selection of Representative Proteins

BLAST (Basic Local Alignment Search Tool) analysis[44] was performed using the UniProtKB database[45] to identify homologous protein sequences. The query protein was reported to exhibit defluorination potential and was associated with UniProt ID Q6NAM1 (RPA1163).[16] It was submitted to the UniProt BLAST server, and searches were conducted against the full UniProtKB data set with default parameters. Proteins exhibiting more than 50% sequence similarity to the query sequence were selected for further analysis. Phylogenetic information for the resulting 184 proteins was retrieved from UniProt. From the 184 identified proteins spanning nine bacterial classes, four representative sequences were selected from the class Alphaproteobacteria due to the high prevalence of this protein family within this class. From each of the remaining classes, a single representative protein was selected based on sequence similarity. The selected proteins include A0A4U5JW23 (Gammaproteobacteria as **P1**), A0A4Z0BVY8 (Betaproteobacteria as **P2**), A0A8J7A8L8 (Cyanophyceae as **P3**), A0A9X3N3I3 (Thermoleophilia as **P4**), A0A172ZIM2 (Bacilli as **P5**), A0A387B7I1 (Actinomycetes as **P6**), A0A447CYM1 (Alphaproteobacteria as **P7**), Q2IYY8 (Alphaproteobacteria as **P8**), A0A1B9Z5E1 (Alphaproteobacteria as **P9**), A0A2W2AYK9 (Alphaproteobacteria as **P10**), A0A7V8CW33 (Chloroflexota as **P11**) and A0A927B728 (Bacteroidota as **P12**) (Table 1).

Sequence Alignment and Structural Comparison

The amino acid sequences of the 12 selected proteins were aligned with the sequence of RPA1163 using MEGA 12 with the BLOSUM62 substitution matrix.[46] The resulting multiple sequence alignment was analyzed to assess residue conservation across the nine bacterial classes using the Alignment Viewer tool.[47] Three-dimensional structures for the majority of the selected proteins were obtained directly from the AlphaFold database.[48,49] For proteins whose structures were not available in the AlphaFold data set (A0A8J7A8L8, A0A9X3N3I3, and A0A927B728), structural models were generated using AlphaFold2 and subsequently evaluated for accuracy based on predicted local distance difference test (pLDDT) scores[50] (SI Figure S1).

The experimentally determined crystal structure of RPA1163 was retrieved from the UniProtKB database and analyzed using ChimeraX version 1.9.[51] The ligand-binding pocket was identified based on previously reported data by Chan et al.[16] Structural analyses of all 12 selected protein models were performed using ChimeraX, and each structure was quantitatively compared to RPA1163 using the MatchMaker tool[52] to evaluate structural similarity.

Molecular Docking

Molecular docking was performed using the Smina software,[53] which employs an empirical and knowledge-based scoring function trained on the CSAR−NRC HiQ 2010 data set.[53] Protein and ligand structures were prepared using the Open Babel package[54] to convert Protein Data Bank (PDB) files into the PDBQT format, incorporating partial atomic charges (Q) and AutoDock 4 (AD4) atom types (T). The binding pocket coordinates for the target proteins were defined based on previously reported structural data by Chan et al.[16] and Kamachi et al.[28] The ligand-binding pose with the most favorable docking score was selected.

Molecular Dynamic Simulation

All MD simulations were performed using the OpenMM simulation engine[55] to evaluate the structural stability and dynamic behavior of the protein−ligand complexes. Protein parameters were described using the AMBER ff14SB[56] force field, while ligand parameters were generated using the General AMBER Force Field (GAFF)[57] with partial atomic charges assigned using the AM1-BCC[58] method. The protein−ligand complexes were solvated in an explicit TIP3P water model[59] within a cubic periodic box, ensuring a minimum distance of 10 Å between any solute atom and the box boundary. Appropriate counterions (Na^+/Cl^-) were added to neutralize the system and achieve a physiological ionic strength of 0.15 M.[60,61]

Prior to production simulations, the system was subjected to a multistep equilibration protocol. Initial energy minimization was carried out using the L-BFGS algorithm[62] to remove steric clashes and unfavorable contacts. The system was then gradually heated from 0 to 300 K for 200 ps under constant volume (NVT) conditions using a Langevin thermostat.[63] This was followed by pressure equilibration for 200 ps under isothermal−isobaric (NPT) conditions at 1 atm using a Monte Carlo barostat,[64] while maintaining a temperature of 300 K. Following equilibration, a 1.2 μs production MD simulation was performed in the NPT ensemble. A time step of 2 fs was employed, with all covalent bonds involving hydrogen atoms

https://doi.org/10.1021/acs.jpcb.6c02887
J. Phys. Chem. B 2026, 130, 7349−7363

constrained using the SHAKE algorithm.[65] Long-range electrostatic interactions were treated using the particle mesh Ewald (PME)[66] method with a real-space cutoff of 10 Å, while the same cutoff was applied for van der Waals interactions with a smooth switching function. Periodic boundary conditions were applied in all three dimensions throughout the simulation. All the calculations were performed in triplicate.[67,68] Trajectory coordinates were saved at regular intervals for subsequent analysis. Structural stability and convergence were assessed using root-mean-square deviation (RMSD), root-mean-square fluctuation (RMSF), and radius of gyration analyses.

QM/MM Analysis

Hybrid QM/MM calculations were carried out using the ONIOM method[69] as implemented in Gaussian 16[70] to obtain an accurate description of protein−ligand interactions and the defluorination active site environment. The system was partitioned into QM and MM layers based on chemical relevance and proximity to the reaction center. The QM region consisted of the ligand, key binding pocket residues Arg111, Arg114, His155, Trp156, Tyr219, and two water molecules. This region was treated at the density functional theory (DFT) level using the ωB97X-D/6−31G(d,p)/AMBER level of theory[71,72] providing a balanced description of electronic structure and computational efficiency. Hydrogen link atoms were employed to cap covalent bonds crossing the QM/MM boundary, following standard ONIOM protocols.

The MM region included the remainder of the protein and surrounding environment and was described using the AMBER ff14SB force field. Ligand parameters in the MM layer were assigned using GAFF, with partial atomic charges derived using the AM1-BCC scheme. Initial QM/MM structures were extracted from the final snapshot of the 1.2 μs molecular dynamics trajectories. Before simulation, all water molecules were deleted, with the exception of two water molecules maintained in the binding pocket to preserve key interactions. After a 2000-step energy minimization, geometry optimizations were performed using the ONIOM scheme while restraining atoms distant from the active site to preserve the overall protein fold. Optimizations were conducted until convergence criteria for energy and forces were satisfied. Subsequently, vibrational frequency calculations were performed on the optimized structures using the same model chemistry. The resulting protein−ligand complexes were confirmed as local minima on the potential energy surface, as verified by frequency calculations.[73] All QM/MM calculations were performed using the mechanical embedding scheme, as implemented in Gaussian 16. The ONIOM energy expression was used consistently to compare protein−ligand interaction strengths across species. The resulting QM/MM descriptors were used to classify and rank defluorination potential relative to the reference system.

Local Vibrational Mode Analysis (LMA)

An important tool we used in this work was the LMA. The underlying theory is described in two comprehensive review articles.[40,74] Therefore, in the following, only the essentials are summarized. Information on the electronic structure of a molecule, in particular the strength of its bonds, is encoded in the normal vibrational modes.[75] However, these modes are generally delocalized, as pointed out by Wilson,[76] due to a coupling of the atomic movements during the vibration, which hinders the direct access to this valuable information. LMA, originally introduced by Konkoli-Cremer[40,74,77,78] provides a unique solution to this problem by extracting local vibrational modes and related local properties from the fundamental normal vibrational modes. The local vibrational modes reflect the local movements of an atomic fragment being described by an internal coordinate such as bond length, bond angle and dihedral angle,[40,74] or special coordinates such as Cremer-Pople ring puckering coordinates.[79] Over the past two decades, we have successfully applied local mode force constants to characterize the strength of covalent bonds and noncovalent interactions across the periodic table, analyzing molecular systems in gas phase, solution and protein environment, as documented in refs 40 and 74. Some more recent applications include the assessment of protein−ligand hydrogen bond strength patterns,[80] weak and strong π interactions in sandwich complexes,[81,82] a revised pK_a rule in light of local mode force constants for the characterization of cocrystals,[83,84] local vibrational mode force constants as features in drug design,[85,86] the characterization of metal−ligand and hydrogen bonding in hemoglobins,[87,88] cytochrome b5,[89] and bacterioferritins,[90] as well as the elucidation of actinide[82,91−94] and lanthanide bonding.[95−99] A local vibrational mode $\mathbf{a}_n$ is defined as

$$\mathbf{a}_n = \frac{\mathbf{K}^{-1}\mathbf{d}_n^{\dagger}}{\mathbf{d}_n\mathbf{K}^{-1}\mathbf{d}_n^{\dagger}} \tag{2}$$

where the two ingredients needed, the diagonal normal mode force constant matrix $\mathbf{K}$ in normal mode coordinates and the normal mode vectors $\mathbf{d}_n$ in internal coordinates, can be obtained from the output of vibrational frequency calculation via the Wilson GF formalism,[75,76,100] a standard procedure in modern quantum chemistry packages.[101] That means, LMA can be applied with minimal computational costs after a routine quantum-chemical calculation of vibrational frequencies, optionally adding measured frequencies as input (a feature opening LMA to the experimental vibrational spectroscopists) to both single molecules in gas phase, solution, or in a protein, but also to periodic systems and crystals.[40,74] For each local mode $\mathbf{a}_n$, one can derive associated local force constants k_n^a describing the local vibration of the atomic fragment under consideration,

$$k_n^a = \mathbf{a}_n^{\dagger}\mathbf{K}\mathbf{a}_n = \frac{1}{\mathbf{d}_n\mathbf{K}^{-1}\mathbf{d}_n^{\dagger}} \tag{3}$$

In this work, we focused on local mode stretching force constants k_n^a(AB) reflecting the intrinsic strength of the bond/interaction between two atoms A and B,[102] with a special emphasis on hydrogen bonding.[80,103−105]

RESULTS AND DISCUSSION

Selection of Representative Proteins

The selected reference protein is a fluoroacetate dehalogenase found in *Rhodopseudomonas palustris* (strain ATCC BAA-98/CGA009). BLAST analysis identified proteins from 186 bacterial species, of which two were taxonomically undefined. The remaining 184 species were distributed across nine bacterial classes. The majority of the sequences (163 species) belonged to the Alphaproteobacteria class. The remaining sequences belonged to Betaproteobacteria (4 species), Gammaproteobacteria (4 species), Cytophagia (1 species), Actinomycetia (7 species), Thermoleophilia (1 species), Cyanophyceae (2 species), Bacilli (1 species), and Chloroflexia (1 species). Notably, all 163 Alphaproteobacterial species belonged to the order Hyphomicrobiales. This strong taxonomic clustering suggests that the protein of interest may have originated within the Alphaproteobacteria−Hyphomicrobiales lineage and was subsequently disseminated to other bacterial classes through horizontal gene transfer or related evolutionary mechanisms. Figure 1 shows the phylogeny of the 186 bacterial species to which the selected proteins belonged. The proteins selected for further analysis are listed in Table 1, along with details of their corresponding bacterial species, taxonomic classes, and sequence similarity to the RPA1163 protein.

Sequence Alignment Analysis

The alignment of the amino acid sequences shows conservation of residues across classes, especially at key binding sites (Table 2).[16] Alignment of the proteins **P7**, **P8**, **P9** and **P10** belonging to bacterial species within class Alphaproteobacteria showed 100% conservation in 111

https://doi.org/10.1021/acs.jpcb.6c02887
J. Phys. Chem. B 2026, 130, 7349−7363

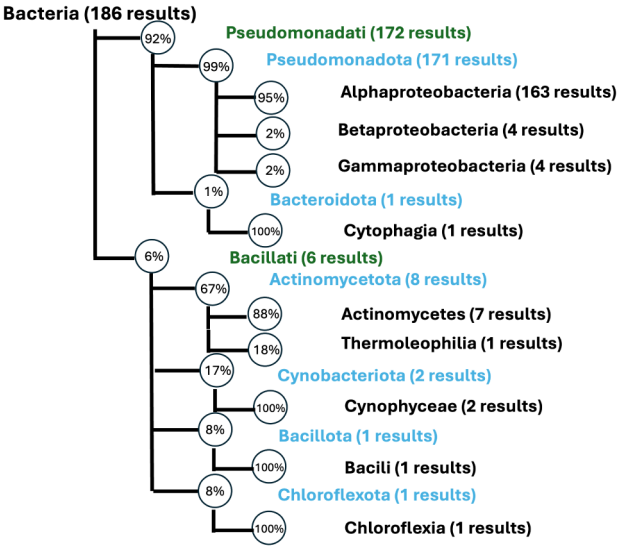

Figure 1. Phylogenetic relationships of bacterial classes and the distribution of bacterial species with proteins from BLAST analysis; which share more than 50% sequence similarity with the protein Q6NAM1 (Reference), among the bacterial classes. The number of species belonging to each class is also shown.

residues out of 310. This suggests the high possibility of the prevalence of defluorinase activity within class Alphaproteobacteria. Proteins **P1**, **P2**, **P7**, **P8**, **P9** and **P10** of bacterial species belonging to the phylum Pseudomonadati showed 100% conservation in 92 residues out of 310. Sequences of all 12 selected proteins showed 100% conservation in 54 residues out of 310. This is a considerably high amount, suggesting the possibility of defluorinase activity in all selected proteins. The sequence alignment of the 12 selected proteins with the reference protein is presented in Figure S2 of the Supporting Information.

Binding Pocket Characterization

The apo structure of wild-type RPA1163 (Reference) adopts a homodimeric architecture with an α/β hydrolase fold, comprising a central $\alpha/\beta/\alpha$ core domain capped by an α-helical subdomain. The conserved catalytic triad, Asp110 (nucleophile), His280 (general base), and Asp134 (carboxylate), defines the active site, which is located at the domain interface and is accessible through an approximately 11 Å long channel with an active site composition Phe40, Arg111, Arg114, His155, Trp156, Trp185, and Tyr219. Moreover, the spatial arrangement of these residues is highly conserved, with a least-squares fit yielding an RMSD of only 0.19 Å. This observation suggests that defluorination requires a highly precise organization of active site residues and bonding geometries.[106,107] Since phenylalanine does not participate in hydrogen bonding and the side-chain nitrogen of Trp185 is oriented away from the binding site, Phe40 and Trp185 were excluded from the binding pocket. This selection is consistent with previous reports in the literature.[28] Table 2 summarizes the composition of the binding pocket and active site residues across the 12 proteins and the reference structure. The results indicate that all proteins exhibit conserved binding pocket and active site compositions, with the exception of P1 and P12, where His155 is substituted by proline.

Substrate binding is represented by the Michaelis complex, in which intact fluoroacetate (FAc) is accommodated within the active site of RPA1163. The reaction mechanism of RPA1163 with FAc has been experimentally elucidated and is well described by Chan et al.[16] Additionally, the reaction mechanism of fluoroacetate dehalogenase has been computationally investigated by Kamachi et al.[28] using QM/MM analysis. Figure 2 illustrates the RPA1163 binding pocket. The catalytic process follows an SN2 mechanism, in which the carboxylate group of Asp110 acts as a nucleophile, attacking the α-carbon of the substrate to displace the fluorine atom and form an ester intermediate. This intermediate is subsequently hydrolyzed by a water molecule activated by His280. In this complex, the carboxylate oxygen atoms of FAc are coordinated by Arg111 (2.7 Å) and Arg114, and additionally stabilized through a hydrogen bond with Tyr219 (2.8 Å). The fluorine atom of FAc interacts with His155 (3.0 Å), Trp156 (3.3 Å), and Tyr219 (3.2 Å), suggesting that these residues contribute to weakening the C−F bond and stabilizing the departing fluoride ion during catalysis.[16]

Protein Structure Analysis and Structural Comparison

Structural similarity between the selected proteins and the reference RPA1163 enzyme was assessed using RMSD values obtained from three-dimensional structural alignments (Figure 3). RMSD values $\leq$ 2 Å indicate high structural similarity and suggest conserved functionality, while values between 2 and 4 Å imply moderate similarity that can still retain activity. RMSD values >4 Å are indicative of potential functional divergence.

Table 2. Binding and Active Site Residue Conservation across Selected Species

	Binding site					Active site		
	111	114	155	156	219	110	134	280
Reference (Alphaproteobacteria)	Arg	Arg	His	Trp	Tyr	Asp	Asp	His
P1 (Gammaproteobacteria)	Arg	Arg	Pro	Trp	Tyr	Asp	Asp	His
P2 (Betaproteobacteria)	Arg	Arg	His	Trp	Tyr	Asp	Asp	His
P3 (Cyanobacteriota)	Arg	Arg	His	Trp	Tyr	Asp	Asp	His
P4 (Thermoleophilia)	Arg	Arg	His	Trp	Tyr	Asp	Asp	His
P5 (Bacillales)	Arg	Arg	His	Trp	Tyr	Asp	Asp	His
P6 (Actinomycetes)	Arg	Arg	His	Trp	Tyr	Asp	Asp	His
P7 (Alphaproteobacteria)	Arg	Arg	His	Trp	Tyr	Asp	Asp	His
P8 (Alphaproteobacteria)	Arg	Arg	His	Trp	Tyr	Asp	Asp	His
P9 (Alphaproteobacteria)	Arg	Arg	His	Trp	Tyr	Asp	Asp	His
P10 (Alphaproteobacteria)	Arg	Arg	His	Trp	Tyr	Asp	Asp	His
P11 (Chloroflexia)	Arg	Arg	His	Trp	Tyr	Asp	Asp	His
P12 (Bacteroidota)	Arg	Arg	Pro	Trp	Tyr	Asp	Asp	His

https://doi.org/10.1021/acs.jpcb.6c02887
J. Phys. Chem. B 2026, 130, 7349−7363

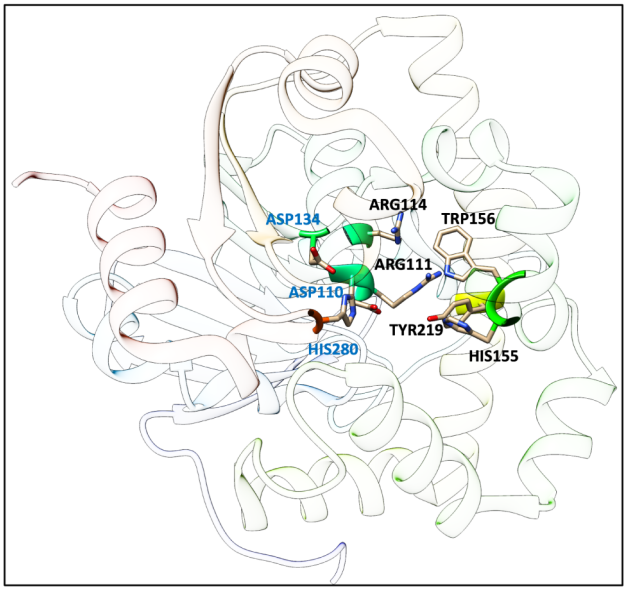

Figure 2. Amino acid residues at the binding site (black) and active site (blue) of RPA1163 (Reference protein).

All selected proteins exhibited RMSD values below 2 Å, indicating substantial structural conservation with RPA1163 (reference). Proteins from Alphaproteobacteria (**P7**, **P8**, **P9** and **P10**) showed particularly strong similarity (RMSD = 0.75−1.37 Å), suggesting a high likelihood of conserved defluorinase activity within this class. Comparable structural similarity was also observed for proteins from Betaproteobacteria, Gammaproteobacteria, Bacteroidota, Actinomycetes, Thermoleophilia, Cyanophyceae, Bacilli, and Chloroflexia, with RMSD values ranging from 1.06 to 1.97 Å (Table 3). Overall, these results indicate that the defluorinase structural fold is well conserved across diverse bacterial classes, supporting the hypothesis that defluorination activity is broadly distributed across phylogenetically distinct species.

Protein Dynamics

Long-time scale (1.2 μs) molecular dynamics (MD) simulations were performed to evaluate the structural stability and dynamic behavior of the reference RPA1163 enzyme and the 12 selected homologous proteins. In the literature, microsecond-scale molecular dynamics simulations are widely employed to capture slow conformational changes, rare events, and realistic protein−ligand interactions that are not accessible on shorter time scales. In the present study, two primary objectives motivated the use of extended simulations.[108,109] First, AI-generated protein structures may contain structural inaccuracies or unresolved artifacts, necessitating long-time scale simulations to ensure adequate structural relaxation and validation. Second, these simulations enable a comprehensive assessment of conformational changes and the dynamic stability of the system. Analysis of the backbone root-mean-square deviation (RMSD) revealed that all 12 proteins, including RPA1163 (Reference), rapidly equilibrated and remained stable throughout the simulation. Backbone RMSD values consistently remained below 2 Å after the initial equilibration phase, indicating the absence of large-scale

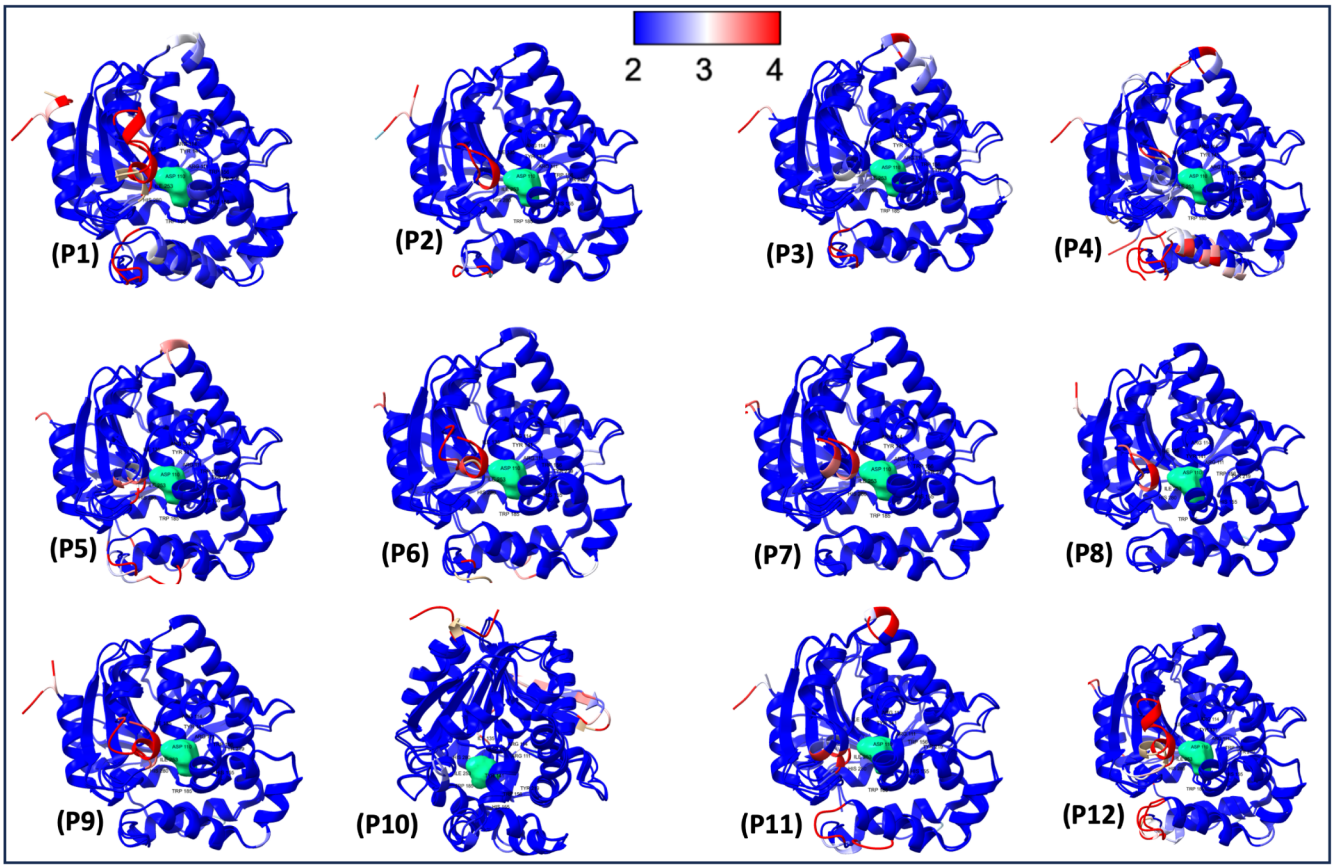

Figure 3. AlphaFold2 generated protein structure alignment with RPA1163 (Reference).

https://doi.org/10.1021/acs.jpcb.6c02887
J. Phys. Chem. B 2026, 130, 7349−7363

Table 3. Summary of RMSD Values of Proteins Aligned with RPA1163

Index	UniProt Accession	Species Name	Class	RMSD Value
1	A0A4U5JW23 (**P1**)	*Luteimonas gilva*	Gammaproteobacteria	1.968
2	A0A4Z0BVY8 (**P2**)	*Ramlibacter rhizophilus*	Betaproteobacteria	1.063
3	A0A8J7A8L8 (**P3**)	*Vasconcelosia minhoensis*	Cyanophyceae	1.130
4	A0A9×3N3I3 (**P4**)	*Solirubrobacter ginsenosidimutans*	Thermoleophilia	1.870
5	A0A172ZIM2 (**P5**)	*Paenibacillus bovis*	Bacilli	1.436
6	A0A387B7I1 (**P6**)	*Protaetiibacter intestinalis*	Actinomycetes	1.248
7	A0A447CYM1 (**P7**)	*Rhodoplanes serenus*	Alphaproteobacteria	0.987
8	Q2IYY8 (**P8**)	*Rhodopseudomonas palustris* (strain HaA2)	Alphaproteobacteria	0.749
9	A0A1B9Z5E1 (**P9**)	*Bradyrhizobium* sp. LMTR 3	Alphaproteobacteria	1.105
10	A0A2W2AYK9 (**P10**)	*Aestuariivirga litoralis*	Alphaproteobacteria	1.371
11	A0A7 V8CW33 (**P11**)	*Chloroflexia bacterium* SDU3−3	Chloroflexia	1.589
12	A0A927B728 (**P12**)	*Spirosoma validum*	Bacteroidota	1.921

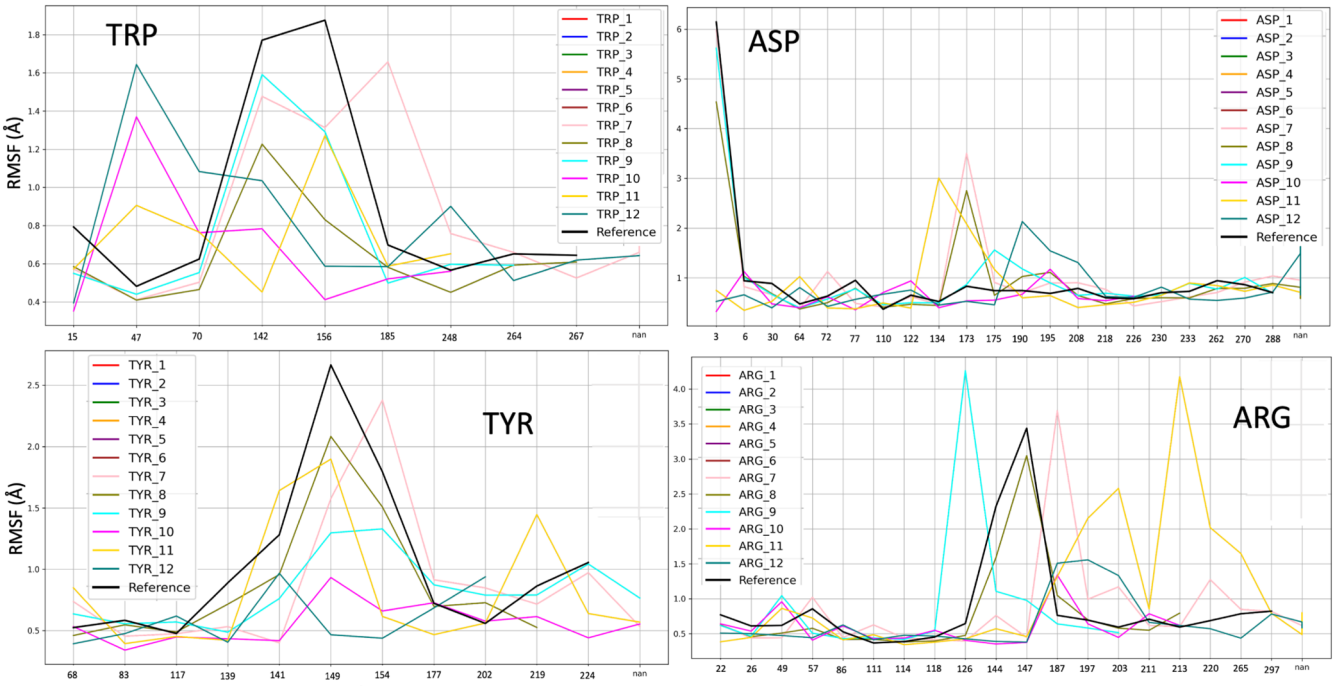

Figure 4. Root mean square fluctuations (RMSF) of Trp, Asp, Tyr, and Arg residues for the reference protein RPA1163 and the corresponding **P1**−**P12** protein−ligand complexes, highlighting residue-level flexibility during 1.2 μs long molecular dynamics simulations.

conformational rearrangements. Our results indicate that the 12 AI-generated models exhibit only small deviations relative to the experimental structure. This observation can be attributed to the overall conservation of the protein fold and the structural constraints imposed by the backbone architecture. Furthermore, contemporary AI-based protein structure prediction methods demonstrate high accuracy in reproducing global structural features, often achieving near-experimental levels of accuracy in backbone conformations.[110,111]

In addition to the RMSD analysis, residue-level flexibility was evaluated using root-mean-square fluctuation (RMSF) analysis. As expected, higher fluctuations were observed primarily in loop regions and terminal residues, while secondary structural elements such as *α-helices* and *β-sheets* exhibited minimal fluctuations. Importantly, residues involved in substrate binding and catalysis displayed low RMSF values across all proteins, indicating a preserved and rigid binding environment. This behavior is consistent with functional conservation and suggests that the dynamic properties of the active site are maintained across species.[112,113] Before discussing and comparing residue-wise deviations obtained from the 1.2 μs molecular dynamics simulations, it is important to note that exact reproduction of experimental values reported by Chan et al.[16] is not expected. Although the experimental study exhibits minimal deviations (≤0.19 Å), molecular dynamics simulations inherently rely on classical force fields and do not explicitly account for electronic structure effects, which limits their ability to reproduce experimental precision. In this study, deviations below 2 Å are considered insufficient to indicate significant structural changes. Accordingly, only residues exhibiting notable deviations throughout the simulation are discussed. However, high-accuracy QM/MM calculations combined with LMA were performed to enable direct comparison with experimental measurements, as described in the following section.

Figure 4 illustrates the dynamic behavior of Trp, Asp, Tyr, and Arg residues over the 1.2 μs molecular dynamics simulations for all 12 protein systems. Tryptophan residues exhibit noticeable, yet restrained, fluctuations below 2 Å, particularly for Trp142 and Trp156 in the reference system.

https://doi.org/10.1021/acs.jpcb.6c02887
J. Phys. Chem. B 2026, 130, 7349−7363

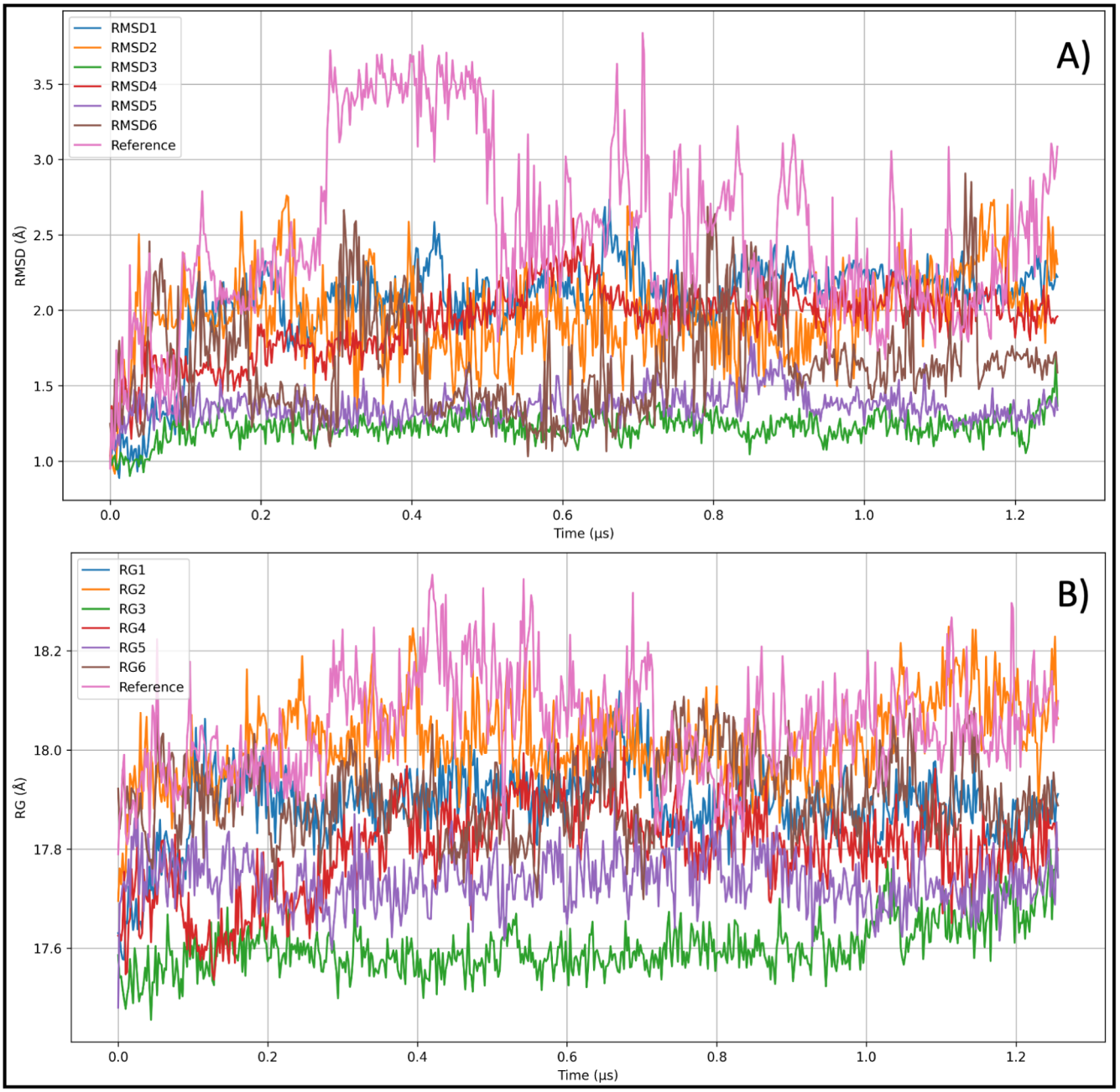

Figure 5. (A) Backbone root-mean-square deviation (RMSD) for the reference protein RPA1163 and the corresponding **P1**−**P6** protein−ligand complexes. (B) Radius of gyration (Rg) profiles for the reference protein RPA1163 and the corresponding **P1**−**P6** protein−ligand complexes during 1.2 μs long molecular dynamics simulations.

Notably, Trp156 is a key binding-pocket residue, and similar dynamic behavior is observed in systems **P7**, **P9**, and **P11**. Tyr147 displays comparable deviations, with consistent patterns seen in systems **P7**, **P8**, **P9**, and **P11**. In contrast, Arg147 in the reference protein shows a more pronounced deviation approaching 3 Å, a trend also observed in **P8**, while analogous fluctuations are detected for Arg118 in **P7**, Arg187 in **P11**, and Arg213 in **P9**. Importantly, the binding-pocket arginine residues Arg111 and Arg114 remain largely stable across all systems. Aspartate residues show minimal deviation in the reference system, with moderate fluctuations observed only for Asp173 in **P7** and **P8** and Asp134 in **P11**. Histidine residues are largely stable, exhibiting only a minor fluctuation for the binding-pocket residue His155. Similar dynamic analyses for Phe, Ile, Gln, and Ala residues are provided in Figure S3 of the Supporting Information.

The radius of gyration (Rg) was monitored to assess global compactness during the simulations. All proteins exhibited stable Rg values with minimal temporal variation, further confirming the absence of unfolding events or significant structural expansion. The similarity of Rg profiles among the 12 proteins and RPA1163 (Reference) indicates that the proteins retain a compact and well-organized tertiary structure over the entire 1.2 μs simulation.[68] The backbone RMSD and radius of gyration (Rg) comparisons for the RPA1163 and P1−P6 complexes are shown in Figure 5A and 5B, respectively, while the corresponding analyses for the **P7**−**P12** complexes

https://doi.org/10.1021/acs.jpcb.6c02887
J. Phys. Chem. B 2026, 130, 7349−7363

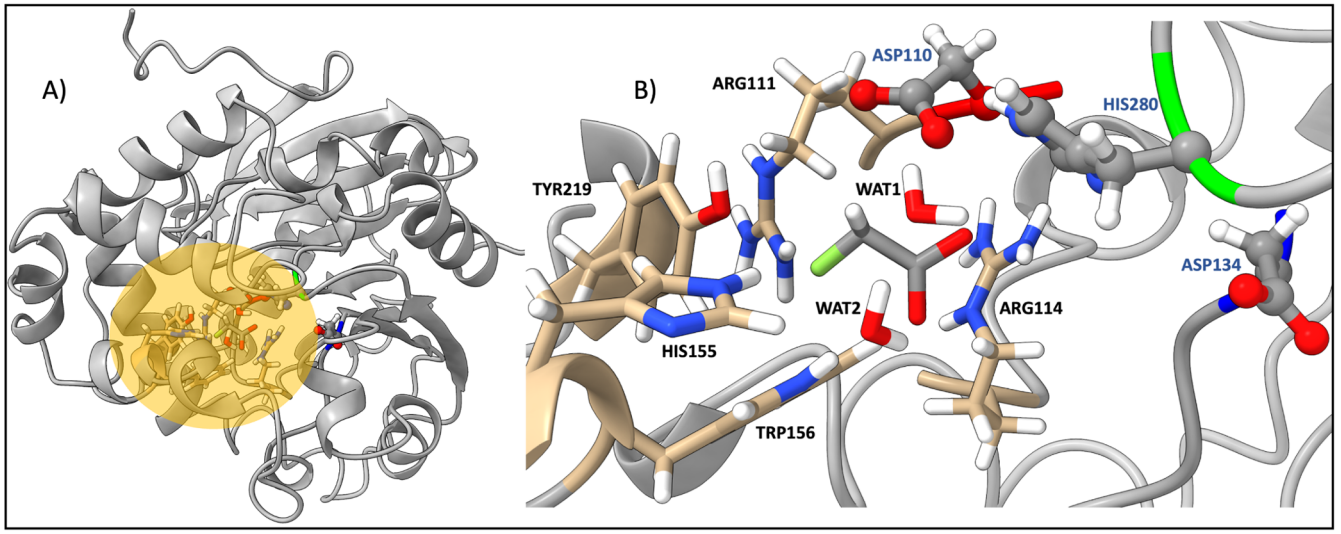

Figure 6. (A) Fluoroacetate dehalogenase from *Rhodopseudomonas palustris* (strain ATCC BAA-98/CGA009), RPA1163, shown in complex with fluoroacetate (FAc). The binding pocket region is highlighted in yellow. (B) Close-up view of the binding pocket illustrating the QM region selected for QM/MM calculations at the ωB97X-D/6−31G(d,p)/AMBER level of theory, including residues Arg111, Arg114, His155, Trp156, and Tyr219, along with two water molecules and FAc. The QM region is shown in stick representation, while the catalytic triad (Asp110, His280, and Asp134) is depicted in ball-and-stick representation with blue name tags.

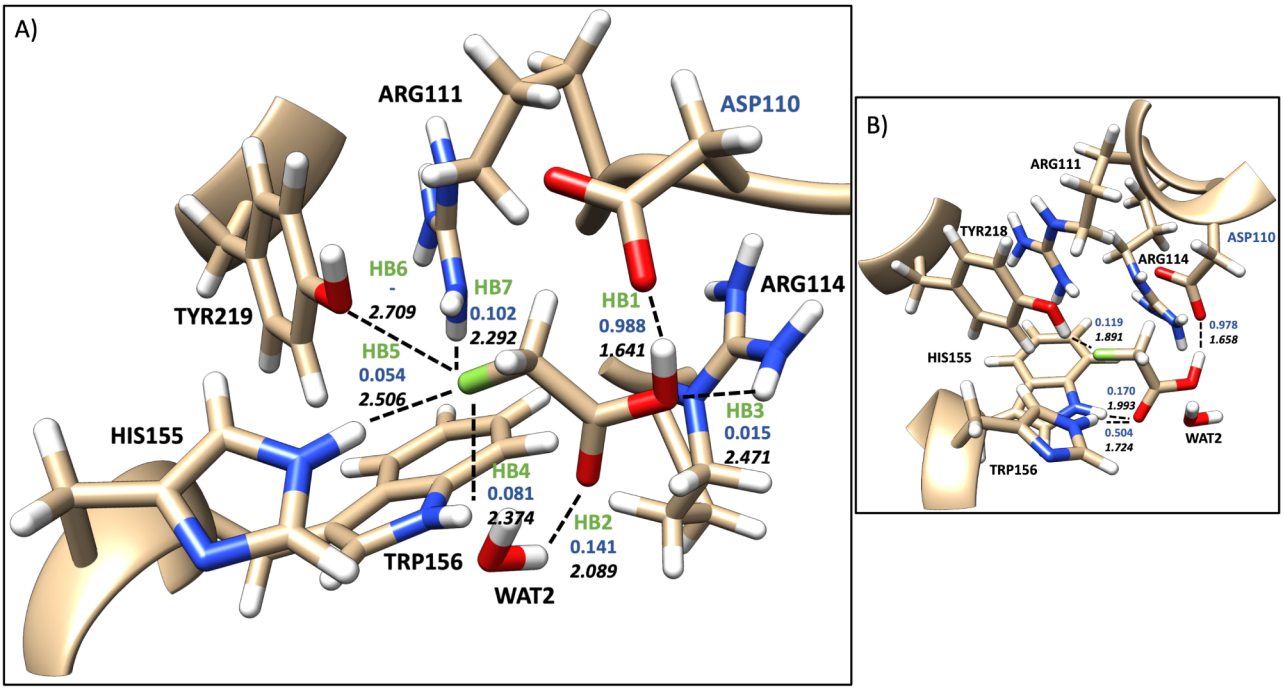

Figure 7. (A) Protein−ligand hydrogen bond representation of the reference structure RPA1163 used for QM/MM and local vibrational mode (LMA) analyses. (B) Corresponding representation for the best-performing protein−ligand complex identified in this study, system **P2** (*Ramlibacter rhizophilus*; class Betaproteobacteria). The values shown in blue indicate the local mode force constant k^a, which quantifies hydrogen bond strength (mDyn/Å), while the values shown in black represent the corresponding hydrogen bond lengths (Å). The HB numbering (green) represents the complete hydrogen-bonding network analyzed across **P1**−**P7** protein−ligand systems.

are provided in Figure S4A and S4B of the Supporting Information.

Collectively, the RMSD, RMSF, and radius of gyration analyses demonstrate that none of the studied proteins deviated by more than 2 Å from their equilibrated structures. These results provide strong evidence that the selected enzymes are dynamically stable and structurally comparable to RPA1163, reinforcing the hypothesis that they may retain similar defluorination functionality. The observed stability across long time scales also validates the use of these structures for subsequent high-level QM/MM and vibrational analyses.

QM/MM and LMA Analysis

QM/MM calculations were employed to achieve an accurate and chemically rigorous description of protein−ligand hydrogen bonding interactions within the binding pocket by treating the ligand, key active-site residues and water molecules at the

https://doi.org/10.1021/acs.jpcb.6c02887
J. Phys. Chem. B 2026, 130, 7349−7363

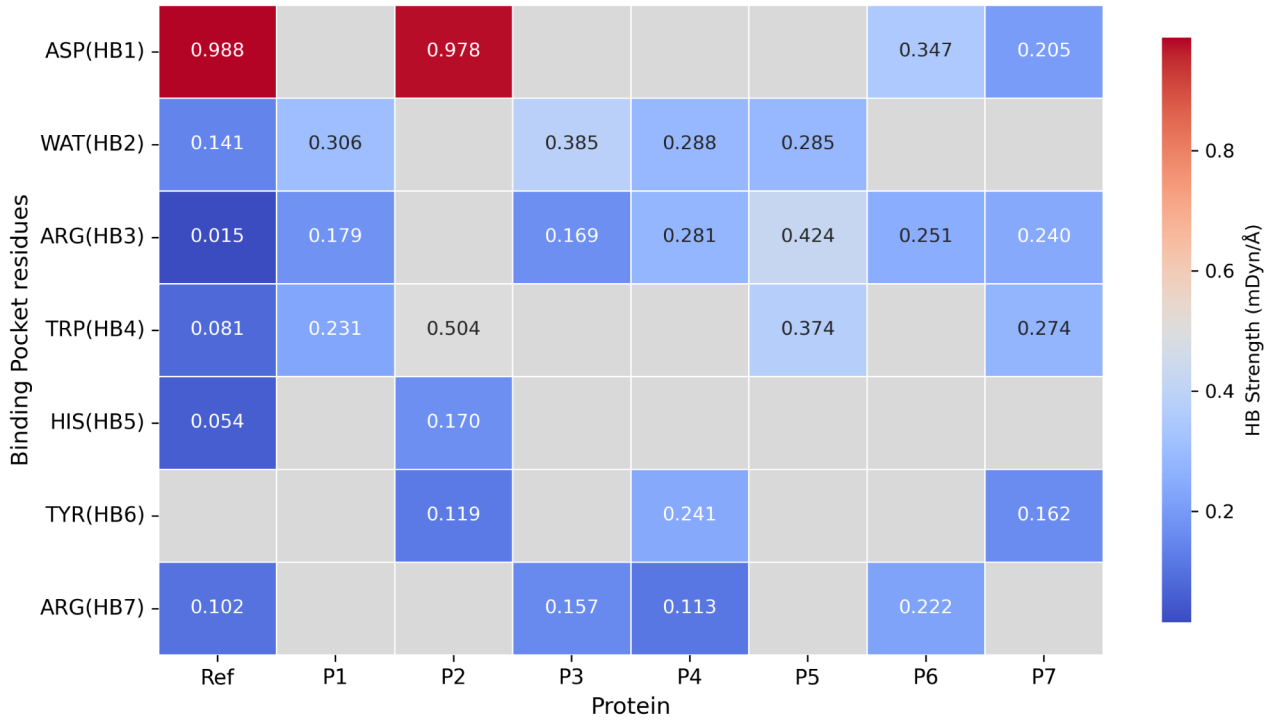

Figure 8. Hydrogen bond strengths for the reference system (RPA1163) and **P1**−**P7** protein−ligand complexes. HB numbering is visualized in Figure 7A. Hydrogen bonds with strengths below 0.100 mDyn/Å are excluded from the heatmap, except for the reference system.

quantum mechanical (QM) level while representing the remaining protein using molecular mechanics (MM), as shown in Figure 6, this hybrid approach captures electronic effects such as polarization, charge transfer, and hydrogen bond directionality that are not fully described by classical force fields.[106,114] On the other hand, the LMA provides a unique, quantitative measure of intrinsic protein−ligand interaction strengths beyond conventional bond length-based descriptors.

Pioneering work by Pauling,[115] Slater,[116] and Mulliken[117] laid the foundation for our understanding of the chemical bond, establishing that bond strength is governed by two primary factors: the degree of overlap between interacting atomic orbitals (covalent character) and the bond's polarity, which is a function of the energy difference between the involved atomic orbitals (ionic character). Bond dissociation enthalpy (BDE)[118] is a standard metric used to quantify the strength of a chemical bond. BDE measures the energy difference between a molecule at its ground-state equilibrium geometry and its dissociated fragments at their own equilibrium geometries. While BDE is a common measure, it is important to note that it is influenced by both the inherent strength of the bond being broken and the stability of the resulting fragments. On the other hand, the complex interplay of electron delocalization in aromatic systems and ring strain in cyclic structures makes BDE less reliable. An alternative approach to describing chemical bond strength, dating back to the 1920s and 1930s, involves the use of stretching force constants. This method was notably advanced by Badger,[119] who established relationships between force constants and bond lengths for diatomic molecules. The strength of a chemical bond can be reliably determined by the dynamic measure of the local bond stretching force constant, k^a. This local stretching mode specifically probes the bond's intrinsic strength, as the stretching force constant corresponds to an infinitesimal change in bond length that does not induce any relevant change in the bond's electronic structure. This approach provides a direct and unambiguous measure of bond strength, making it particularly useful in various scenarios.[120]

Although experimental data report six hydrogen bond interactions, all associated donor−acceptor distances exceed 2.7 Å.[16] Hydrogen bonds with lengths greater than 2.3 Å typically correspond to very weak interactions. Consistent with our previous studies, these hydrogen bonds generally exhibit k^a values below 0.1 mDyn/Å.[80,104,121] For example, as shown in Figure 7A, in HB3, the bond length of 2.471 Å corresponds to a weak interaction strength of 0.015 mDyn/Å. However, we have reproduced Figure 4B from Chan et al.[122] incorporating both experimental bond distances and the corresponding values obtained after docking, 1.2 μs molecular dynamics simulations, and QM/MM geometry optimization. The close agreement among these results is presented in Figure S5 of the Supporting Information, which confirms only minor deviations in orientation relative to the experimental structure. The primary objective of this study is not to reestablish the reaction mechanism between RPA1163 and FAc, which has been previously elucidated, but rather to identify and compare enzymes with similar functionality across different bacterial species. Our analysis focuses on conserved interaction patterns. Here, we analyze seven protein−ligand hydrogen bonds identified in the reference system (Figure 7A) and compare them across P1−P7 bacterial species. The corresponding hydrogen bond strengths are mapped for eight systems, as shown in Figure 8. Hydrogen bonds with strengths below 0.100 mDyn/Å are classified as weak interactions; therefore, such interactions are retained only for the reference system to clearly define the seven hydrogen bonds.

Eight protein−ligand systems, including the reference, RPA1163, are consistent with experimental hydrogen bond distances by Chan et al.[16] exhibiting weak hydrogen bonding

https://doi.org/10.1021/acs.jpcb.6c02887
J. Phys. Chem. B 2026, 130, 7349−7363

interactions between the fluorine atom of FAc and residues Tyr219, Trp156, and His155. In contrast, several systems display comparatively stronger interactions, as illustrated in the hydrogen-bond strength heat map (Figure 8), notably in systems **P2**, **P4**, **P6**, and **P7**. QM/MM and LMA Results reveal an additional hydrogen bond between the hydroxyl oxygen (−OH) of FAc and Asp110, which constitutes a particularly strong interaction in the reference system, with a local mode force constant (k^a) of 0.998 mDyn/Å and a bond length of 1.641 Å. Comparable interaction strengths were observed in system **P2** (k^a = 0.978 mDyn/Å), with moderately strong interactions in **P6** (0.347 mDyn/Å) and **P7** (0.205 mDyn/Å). In addition, two recurring hydrogen bonds involving a conserved water molecule and Arg111 were detected across most systems. The combined QM/MM and LMA results indicate that system **P2** (*Ramlibacter rhizophilus*, which belongs to the class Betaproteobacteria) exhibits the strongest correlation with the reference enzyme, as shown in Figure 7, followed by **P6** (*Protaetiibacter intestinalis*; class Actinomycetota) and **P7** (*Rhodoplanes serenus*; class Alphaproteobacteria).

CONCLUSION

We have developed and successfully applied a multistep computational workflow for the identification and characterization of fluoroacetate dehalogenase-like enzymes across diverse bacterial species, demonstrating its general applicability to other protein systems. The results further indicate that AlphaFold-generated protein structures provide reliable starting models for large-scale screening and mechanistic investigations, particularly in capturing conserved structural features. Combined with BLAST, molecular dynamics simulations, QM/MM and local vibrational mode analysis (LMA), this workflow enables robust assessment of protein−ligand interactions and functional conservation, offering a scalable framework for enzyme discovery and characterization. Molecular dynamics analyses reveal well-defined and stable residue-level behavior for both the reference enzyme and the 12 homologous systems. Together with the conservation of binding-site residues and the high structural similarity (RMSD < 2 Å), these results suggest that all 12 proteins possess the potential to function as defluorinase enzymes.

The resulting protein−ligand interaction patterns are consistent with experimentally reported observations by Chan et al.[16] Among the analyzed systems, **P2** (*Ramlibacter rhizophilus*; class Betaproteobacteria) exhibits the closest agreement with the reference enzyme (RPA1163) in terms of structural, dynamical, and interaction-level features, followed by **P6** (*Protaetiibacter intestinalis*; class Actinomycetota) and **P7** (*Rhodoplanes serenus*; class Alphaproteobacteria). Furthermore, these findings suggest the presence of defluorination capability in five additional bacterial classes, thereby expanding beyond the four classes previously reported.

Future computational mechanistic studies will be essential to elucidate the energetics and provide a detailed understanding of the underlying reaction pathways. In parallel, the identified organisms with potential defluorination activity can be isolated and cultured in media containing fluoroacetate and other fluorinated compounds. Such experimental studies would enable the evaluation of their defluorination efficiency across diverse substrates, as well as their tolerance to reaction products and byproducts. This approach will also facilitate the identification of key reaction intermediates and validation of proposed mechanisms. Upon confirming their defluorination capability, these organisms may be directly applied for the bioremediation of fluorinated pollutants, including PFAS compounds, or serve as sources for the extraction and characterization of defluorinase enzymes.

Overall, this work establishes a robust and transferable computational protocol for identifying and characterizing enzymes with defluorination potential. The methodology presented here can be broadly applied to screen and investigate additional species for functional similarity to a known reference protein, thereby supporting future efforts in bioremediation research.

ASSOCIATED CONTENT

Supporting Information

The Supporting Information is available free of charge at https://pubs.acs.org/doi/10.1021/acs.jpcb.6c02887.

1 Three-dimensional structures of proteins P1−P12, colored according to pLDDT values; (2) amino acid sequence alignment; (3) RMSF analysis for Phe, Ile, Gln, and Ala; (4) RMSD and radius of gyration analysis for **P7−P12;** (5) comparison of experimental and computational values (PDF)

AUTHOR INFORMATION

Corresponding Authors

Eustace Fernando − *Department of Biological Sciences, Rajarata University of Sri Lanka, Mihintale 50300, Sri Lanka*; Email: eustace6192@as.rjt.ac.lk

Elfi Kraka − *Department of Chemistry, Southern Methodist University, Dallas, Texas 75205, United States;* orcid.org/0000-0002-9658-5626; Email: ekraka@smu.edu

Authors

Ayesh Madushanka − *Department of Chemistry, Southern Methodist University, Dallas, Texas 75205, United States*

Chamindu Jayathilake − *Department of Biological Sciences, Rajarata University of Sri Lanka, Mihintale 50300, Sri Lanka*

Nipuni Prematthilaka − *Department of Biological Sciences, Rajarata University of Sri Lanka, Mihintale 50300, Sri Lanka*

Complete contact information is available at: https://pubs.acs.org/10.1021/acs.jpcb.6c02887

Notes

The authors declare no competing financial interest.

ACKNOWLEDGMENTS

This work used resources from the O'Donnell Data Science and Research Computing Institute at Southern Methodist University. The authors declare that no specific financial support was received for this work.

REFERENCES

(1) Butler, A.; Sandy, M. Mechanistic considerations of halogenating enzymes. *Nature* **2009**, *460*, 848−854.

(2) O'Hagan, D. Understanding organofluorine chemistry. An introduction to the C−F bond. *Chem. Soc. Rev.* **2008**, *37*, 308−319.

(3) Lemal, D. M. Perspective on fluorocarbon chemistry. *J. Org. Chem.* **2004**, *69*, 1−11.
(4) Douvris, C.; Ozerov, O. V. Hydrodefluorination of perfluoroalkyl groups using silylium-carborane catalysts. *Science* **2008**, *321*, 1188−1190.
(5) Gaines, L. G. Historical and current usage of per-and polyfluoroalkyl substances (PFAS): A literature review. *Am. J. Ind. Med.* **2023**, *66*, 353−378.
(6) Wang, Z.; DeWitt, J. C.; Higgins, C. P.; Cousins, I. T. A Never-Ending Story of Per- and Polyfluoroalkyl Substances (PFASs)? *Environ. Sci. Technol.* **2017**, *51*, 2508−2518.
(7) U.S. Department of Health and Human Services *Hazardous Substances Data Bank (HSDB, Online Database). National Toxicology Information Program, National Library of Medicine*; U.S. Department of Health and Human Services, 1993.
(8) Glüge, J.; Scheringer, M.; Cousins, I. T.; DeWitt, J. C.; Goldenman, G.; Herzke, D.; Lohmann, R.; Ng, C. A.; Trier, X.; Wang, Z. An overview of the uses of per-and polyfluoroalkyl substances (PFAS). *Environ. Sci.: Processes Impacts* **2020**, *22*, 2345−2373.
(9) Evich, M. G.; Davis, M. J. B.; McCord, J. P.; Acrey, B.; Awkerman, J. A.; Knappe, D. R. U.; Lindstrom, A. B.; Speth, T. F.; Tebes-Stevens, C.; Strynar, M. J.; et al. Per- and Polyfluoroalkyl Substances in the Environment. *Science* **2022**, *375* (6580), No. eabg9065.
(10) Cousins, I. T.; DeWitt, J. C.; Glüge, J.; Goldenman, G.; Herzke, D.; Lohmann, R.; Miller, M.; Ng, C. A.; Scheringer, M.; Vierke, L.; Wang, Z. Strategies for Grouping Per- and Polyfluoroalkyl Substances (PFAS) to Protect Human and Environmental Health. *Environ. Sci.: Processes Impacts* **2020**, *22*, 1444−1460.
(11) Ankley, G. T.; Cureton, P.; Hoke, R. A.; Houde, M.; Kumar, A.; Kurias, J.; Lanno, R.; McCarthy, C.; Newsted, J.; Salice, C. J.; Sample, B. E.; Sepúlveda, M. S.; Steevens, J.; Valsecchi, S. Assessing the Ecological Risks of Per- and Polyfluoroalkyl Substances: Current State-of-the Science and a Proposed Path Forward. *Environ. Toxicol. Chem.* **2020**, *40*, 564−605.
(12) Zhang, Z.; Sarkar, D.; Biswas, J. K.; Datta, R. Biodegradation of per-and polyfluoroalkyl substances (PFAS): A review. *Bioresour. Technol.* **2022**, *344*, 126223.
(13) Hiyama, T. *Organofluorine Compounds: chemistry and Applications*; Springer, 2013.
(14) Ogawa, Y.; Tokunaga, E.; Kobayashi, O.; Hirai, K.; Shibata, N. Current Contributions of Organofluorine Compounds to the Agrochemical Industry. *iScience* **2020**, *23*, 101467.
(15) Seong, H. J.; Kwon, S. W.; Seo, D.-C.; Kim, J.-H.; Jang, Y.-S. Enzymatic defluorination of fluorinated compounds. *Appl. Biol. Chem.* **2019**, *62* (1), 62.
(16) Chan, P. W.; Yakunin, A. F.; Edwards, E. A.; Pai, E. F. Mapping the reaction coordinates of enzymatic defluorination. *J. Am. Chem. Soc.* **2011**, *133*, 7461−7468.
(17) Amaya, G. M.; Durandis, R.; Bourgeois, D. S.; Perkins, J. A.; Abouda, A. A.; Wines, K. J.; Mohamud, M.; Starks, S. A.; Daniels, R. N.; Jackson, K. D. Cytochromes P450 1A2 and 3A4 Catalyze the Metabolic Activation of Sunitinib. *Chem. Res. Toxicol.* **2018**, *31*, 570−584.
(18) Burnham, E. A.; Abouda, A. A.; Bissada, J. E.; Nardone-White, D. T.; Beers, J. L.; Lee, J.; Vergne, M. J.; Jackson, K. D. Interindividual Variability in Cytochrome P450 3A and 1A Activity Influences Sunitinib Metabolism and Bioactivation. *Chem. Res. Toxicol.* **2022**, *35*, 792−806.
(19) Zhang, Y.; Mokkawes, T.; de Visser, S. P. Insights into Cytochrome P450 Enzyme Catalyzed Defluorination of Aromatic Fluorides. *Angew. Chem., Int. Ed.* **2023**, *62* (42), No. e202310785.
(20) Malewschik, T.; Ghiladi, R. A. Dehaloperoxidase: An Enzymatic Swiss Army Knife. *Coord. Chem. Rev.* **2021**, *441*, 213976.
(21) Sorokin, A. B. *Advances in Inorganic Chemistry*; Academic Press, 2022, Vol. *79*; pp. 23−63.
(22) Zhang, Y.; Cao, Y.; Sastri, C. V.; de Visser, S. P. Defluorination of Fluorophenols by a Heme Dehaloperoxidase: Insights into the Defluorination Mechanism. *ACS Catal.* **2025**, *15*, 3898−3912.
(23) Wang, Y.; Liu, A. Carbon−Fluorine Bond Cleavage Mediated by Metalloenzymes. *Chem. Soc. Rev.* **2020**, *49*, 4906−4925.
(24) Huang, Q.; Zhang, X.; Chen, Q.; Tian, S.; Tong, W.; Zhang, W.; Chen, Y.; Ma, M.; Chen, B.; Wang, B.; Wang, J.-B. Discovery of a P450-Catalyzed Oxidative Defluorination Mechanism toward Chiral Organofluorines: Uncovering a Hidden Pathway. *ACS Catal.* **2022**, *12*, 265−272.
(25) Miranda-Rojas, S.; Fernandez, I.; Kaestner, J.; Toro-Labbé, A.; Mendizabal, F. Unraveling the nature of the catalytic power of fluoroacetate dehalogenase. *ChemCatChem* **2018**, *10*, 1052−1063.
(26) Donnelly, C.; Murphy, C. D. Purification and properties of fluoroacetate dehalogenase from Pseudomonas fluorescens DSM 8341. *Biotechnol. Lett.* **2009**, *31*, 245−250.
(27) Jitsumori, K.; Omi, R.; Kurihara, T.; Kurata, A.; Mihara, H.; Miyahara, I.; Hirotsu, K.; Esaki, N. X-Ray crystallographic and mutational studies of fluoroacetate dehalogenase from Burkholderia sp. strain FA1. *J. Bacteriol.* **2009**, *191*, 2630−2637.
(28) Kamachi, T.; Nakayama, T.; Shitamichi, O.; Jitsumori, K.; Kurihara, T.; Esaki, N.; Yoshizawa, K. The catalytic mechanism of fluoroacetate dehalogenase: a computational exploration of biological dehalogenation. *Chem.−Eur. J.* **2009**, *15* (30), 7394−7403.
(29) Mabutyana, L.; Pott, R. W. Photo-fermentative hydrogen production by Rhodopseudomonas palustris CGA009 in the presence of inhibitory compounds. *Int. J. Hydrogen Energy* **2021**, *46*, 29088−29099.
(30) Kathol, M. W. *Developing a Metabolic Engineering Chassis From a Metabolically Versatile Organism, Rhodopseudomonas palustris CGA009*, Ph.D. thesis; The University of Nebraska-Lincoln, 2025.
(31) Kathol, M.; Chowdhury, N. B.; Immethun, C.; Alsiyabi, A.; Morris, D.; Naldrett, M. J.; Saha, R. High enzyme promiscuity in lignin degradation mechanisms in Rhodopseudomonas palustris CGA009. *Appl. Environ. Microbiol.* **2025**, *91* (8), No. e0057325.
(32) Zhao, C.; Zhang, Y.; Chan, Z.; Chen, S.; Yang, S. Insights into arsenic multi-operons expression and resistance mechanisms in Rhodopseudomonas palustris CGA009. *Front. Microbiol.* **2015**, *6*, 986.
(33) Kawasaki, H.; Tone, N.; Tonomura, K. Plasmid-determined dehalogenation of haloacetates in Moraxella species. *Agric. Biol. Chem.* **1981**, *45*, 29−34.
(34) Davis, C. K.; Webb, R. I.; Sly, L. I.; Denman, S. E.; McSweeney, C. S. Isolation and survey of novel fluoroacetate-degrading bacteria belonging to the phylum Synergistetes. *FEMS Microbiol. Ecol.* **2012**, *80*, 671−684.
(35) Rose, P. W.; Prlic, A.; Altunkaya, A.; Bi, C.; Bradley, A. R.; Christie, C. H.; Di Costanzo, L.; Duarte, J. M.; Dutta, S.; Feng, Z.; et al. The RCSB Protein Data Bank: Integrative View of Protein, Gene and 3D Structural Information. *Nucleic Acids Res.* **2017**, *45* (D1), D271−D281.
(36) Agarwal, V.; McShan, A. C. The power and pitfalls of AlphaFold2 for structure prediction beyond rigid globular proteins. *Nat. Chem. Biol.* **2024**, *20*, 950−959.
(37) Kim, Y.; Sim, M.; Lee, M.; Kim, S.; Song, S.; Burke, K.; Sim, E. Extending Density-Corrected Density Functional Theory to Large Molecular Systems. *J. Phys. Chem. Lett.* **2025**, *16*, 939−947.
(38) Hillers-Bendtsen, A. E.; Martínez, T. J. Accelerating Hartree−Fock and Density Functional Theory Calculations Using Tensor Hypercontraction. *J. Chem. Theory Comput.* **2025**, *21*, 11595−11603.
(39) Thiel, W. QM/MM methodology: fundamentals, scope, and limitations. *Multiscale Simul. Methods Mol. Sci.* **2009**, *42*, 203−214.
(40) Kraka, E.; Zou, W.; Tao, Y. Decoding Chemical Information from Vibrational Spectroscopy Data: Local Vibrational Mode Theory. *WIREs Comput. Mol. Sci.* **2020**, *10*, 1480.
(41) Kuhlman, B. Designing protein structures and complexes with the molecular modeling program Rosetta. *J. Biol. Chem.* **2019**, *294*, 19436−19443.
(42) Bertoline, L. M. F.; Lima, A. N.; Krieger, J. E.; Teixeira, S. K. Before and after AlphaFold2: An overview of protein structure prediction. *Front. Bioinform* **2023**, *3*, 1120370.
(43) Li, M. Q. C.; Wang, S.; Lin, S.-R.; Ting, L. E. N.; Wan, Z.-H.; Xie, G.; Zhang, J. Advantages and Limitations of AlphaFold in

Structural Biology: Insights from Recent Studies. *Protein J.* **2026**, *45*, 22−38.
(44) Altschul, S. F.; Gish, W.; Miller, W.; Myers, E. W.; Lipman, D. J. Basic local alignment search tool. *J. Mol. Biol.* **1990**, *215*, 403−410.
(45) Consortium, T. U.; Martin, M.-J.; Orchard, S.; Magrane, M.; Adesina, A.; Ahmad, S.; Bowler-Barnett, E. H.; Bye-A-Jee, H.; Carpentier, D.; Denny, P.; et al. UniProt: the universal protein knowledgebase in 2025. *Nucleic Acids Res.* **2025**, *53* (D1), D609−D617.
(46) Tamura, K.; Stecher, G.; Kumar, S. MEGA11: molecular evolutionary genetics analysis version 11. *Mol. Biol. Evol.* **2021**, *38*, 3022−3027.
(47) *Alignment Viewer Development Team, Alignment Viewer*; 2024. https://alignmentviewer.org, Accessed: 05 January 2026.
(48) Varadi, M.; Bertoni, D.; Magana, P.; Paramval, U.; Pidruchna, I.; Radhakrishnan, M.; Tsenkov, M.; Nair, S.; Mirdita, M.; Yeo, J.; Kovalevskiy, O.; Tunyasuvunakool, K.; Laydon, A.; Zidek, A.; Tomlinson, H.; Hariharan, D.; Abrahamson, J.; Green, T.; Jumper, J.; Birney, E.; Steinegger, M.; Hassabis, D.; Velankar, S. AlphaFold Protein Structure Database in 2024: Providing Structure Coverage for over 214 Million Protein Sequences. *Nucleic Acids Res.* **2024**, *52*, D368−D375.
(49) Varadi, M.; Anyango, S.; Deshpande, M.; Nair, S.; Natassia, C.; Yordanova, G.; Yuan, D.; Stroe, O.; Wood, G.; Laydon, A.; Zidek, A.; Green, T.; Tunyasuvunakool, K.; Petersen, S.; Jumper, J.; Clancy, E.; Green, R.; Vora, A.; Lutfi, M. W.; Figurnov, M.; Cowie, A.; Hobbs, N.; Kohli, P.; Kleywegt, G.; Birney, E.; Hassabis, D.; Velankar, S. AlphaFold Protein Structure Database: Massively Expanding the Structural Coverage of Protein-Sequence Space with High-Accuracy Models. *Nucleic Acids Res.* **2022**, *50*, D439−D444.
(50) Carugo, O. pLDDT values in AlphaFold2 protein models are unrelated to globular protein local flexibility. *Crystals* **2023**, *13*, 1560.
(51) Meng, E. C.; Goddard, T. D.; Pettersen, E. F.; Couch, G. S.; Pearson, Z. J.; Morris, J. H.; Ferrin, T. E. UCSF ChimeraX: Tools for structure building and analysis. *Protein Sci.* **2023**, *32* (11), No. e4792.
(52) Meng, E. C.; Pettersen, E. F.; Couch, G. S.; Huang, C. C.; Ferrin, T. E. Tools for integrated sequence-structure analysis with UCSF Chimera. *BMC Bioinf.* **2006**, *7* (1), 339.
(53) Koes, D. R.; Baumgartner, M. P.; Camacho, C. J. Lessons learned in empirical scoring with smina from the CSAR 2011 benchmarking exercise. *J. Chem. Inf. Model.* **2013**, *53*, 1893−1904.
(54) O'Boyle, N. M.; Banck, M.; James, C. A.; Morley, C.; Vandermeersch, T.; Hutchison, G. R. Open Babel: An open chemical toolbox. *J. Cheminf.* **2011**, *3*, 33.
(55) Eastman, P.; Swails, J.; Chodera, J. D.; McGibbon, R. T.; Zhao, Y.; Beauchamp, K. A.; Wang, L.-P.; Simmonett, A. C.; Harrigan, M. P.; Stern, C. D.; Wiewiora, R. P.; Brooks, B. R.; Pande, V. S. OpenMM 7: Rapid Development of High Performance Algorithms for Molecular Dynamics. *PLoS Comput. Biol.* **2017**, *13*, No. e1005659.
(56) Hornak, V.; Abel, R.; Okur, A.; Strockbine, B.; Roitberg, A.; Simmerling, C. Comparison of multiple Amber force fields and development of improved protein backbone parameters. *Proteins* **2006**, *65*, 712−725.
(57) Wang, J.; Wolf, R. M.; Caldwell, J. W.; Kollman, P. A.; Case, D. A. Development and testing of a general amber force field. *J. Comput. Chem.* **2004**, *25*, 1157−1174.
(58) Jakalian, A.; Jack, D. B.; Bayly, C. I. Fast, efficient generation of high-quality atomic charges. AM1-BCC model: II. Parameterization and validation. *J. Comput. Chem.* **2002**, *23*, 1623−1641.
(59) Jorgensen, W. L.; Chandrasekhar, J.; Madura, J. D.; Impey, R. W.; Klein, M. L. Comparison of simple potential functions for simulating liquid water. *J. Chem. Phys.* **1983**, *79*, 926−935.
(60) Shrimpton-Phoenix, E.; Notari, E.; Kluonis, T.; Wood, C. W. drMD: molecular dynamics for experimentalists. *J. Mol. Biol.* **2025**, *437*, 168918.
(61) Martínez, F. D. P.; Galván-Ciprés, Y.; Colín-Lozano, B.Molecular Simulation in Drug Design: An Overview of Molecular Dynamics Methods*Applied Computer-Aided Drug Design: Models and Methods*Bentham Science2023202−257
(62) Liu, D. C.; Nocedal, J. On the limited memory BFGS method for large scale optimization. *Math. Program.* **1989**, *45*, 503−528.
(63) Gronbech-Jensen, N.; Farago, O. A simple and effective Verlet-type algorithm for simulating Langevin dynamics. *Mol. Phys.* **2013**, *111*, 983−991.
(64) Vandenhaute, S.; Rogge, S. M.; Van Speybroeck, V. Large-scale molecular dynamics simulations reveal new insights into the phase transition mechanisms in MIL-53 (Al). *Front. Chem.* **2021**, *9*, 718920.
(65) Kräutler, V.; Van Gunsteren, W. F.; Hünenberger, P. H. A fast SHAKE algorithm to solve distance constraint equations for small molecules in molecular dynamics simulations. *J. Comput. Chem.* **2001**, *22*, 501−508.
(66) Harvey, M.; De Fabritiis, G. An implementation of the smooth particle mesh Ewald method on GPU hardware. *J. Chem. Theory Comput.* **2009**, *5*, 2371−2377.
(67) Liu, X.; Shi, D.; Zhou, S.; Liu, H.; Liu, H.; Yao, X. Molecular dynamics simulations and novel drug discovery. *Expert Opin. Drug Discovery* **2018**, *13*, 23−37.
(68) Madushanka, A.; Verma, N.; Freindorf, M.; Kraka, E. Papaya Leaf Extracts as Potential Dengue Treatment: An In-Silico Study. *Int. J. Mol. Sci.* **2022**, *23* (20), 12310.
(69) Chung, L. W.; Sameera, W. M. C.; Ramozzi, R.; Page, A. J.; Hatanaka, M.; Petrova, G. P.; Harris, T. V.; Li, X.; Ke, Z.; Liu, F.; Li, H.-B.; Ding, L.; Morokuma, K. The ONIOM Method and Its Applications. *Chem. Rev.* **2015**, *115*, 5678−5796.
(70) Frisch, M. J.; Trucks, G. W.; Schlegel, H. B.; Scuseria, G. E.; Robb, M. A.; Cheeseman, J. R.; Scalmani, G.; Barone, V.; Petersson, G. A.; Nakatsuji, H., et al. *Gaussian 16, Revision C.01*; Gaussian, Inc.: Wallingford, CT, 2016.
(71) Chai, J.-D.; Head-Gordon, M. Systematic optimization of long−range corrected hybrid density functionals. *J. Chem. Phys.* **2008**, *128* (8), 084106.
(72) Ditchfield, R.; Hehre, W. J.; Pople, J. A. Self−Consistent Molecular−Orbital Methods. IX. An Extended Gaussian−Type Basis for Molecular−Orbital Studies of Organic Molecules. *J. Chem. Phys.* **1971**, *54*, 724−728.
(73) Jensen, F. *Introduction to Computational Chemistry*, 3rd ed.; Wiley, 2017.
(74) Kraka, E.; Quintano, M.; La Force, H. W.; Antonio, J. J.; Freindorf, M. The Local Vibrational Mode Theory and Its Place in the Vibrational Spectroscopy Arena. *J. Phys. Chem. A* **2022**, *126*, 8781−8798.
(75) Wilson, E. B.; Decius, J. C.; Cross, P. C. *Molecular Vibrations: the Theory of Infrared and Raman Vibrational Spectra*; McGraw-Hill: New York, 1955.
(76) Wilson, E. B. Some Mathematical Methods for the Study of Molecular Vibrations. *J. Chem. Phys.* **1941**, *9*, 76−84.
(77) Konkoli, Z.; Cremer, D. A New Way of Analyzing Vibrational Spectra. I. Derivation of Adiabatic Internal Modes. *Int. J. Quantum Chem.* **1998**, *67*, 1−9.
(78) Konkoli, Z.; Larsson, J. A.; Cremer, D. A New Way of Analyzing Vibrational Spectra. II. Comparison of Internal Mode Frequencies. *Int. J. Quantum Chem.* **1998**, *67*, 11−27.
(79) Cremer, D.; Pople, J. A. General Definition of Ring Puckering Coordinates. *J. Am. Chem. Soc.* **1975**, *97*, 1354−1358.
(80) Madushanka, A.; Moura, R. T., Jr.; Verma, N.; Kraka, E. Quantum Mechanical Assessment of Protein−Ligand Hydrogen Bond Strength Patterns: Insights from Semiempirical Tight-Binding and Local Vibrational Mode Theory. *Int. J. Mol. Sci.* **2023**, *24* (7), 6311.
(81) Zou, W.; Freindorf, M.; Oliveira, V.; Tao, Y.; Kraka, E. Weak and strong π interactions between two monomers—assessed with local vibrational mode theory. *Can. J. Chem.* **2023**, *101* (9), 616−632.
(82) Peluzo, B. M. T. C.; Makoś, M. Z.; Moura, R. T., Jr.; Freindorf, M.; Kraka, E. Linear versus Bent Uranium(II) Metallocenes − A Local Vibrational Mode Study. *Inorg. Chem.* **2023**, *62*, 12510−12524.
(83) Quintano, M.; Moura, R. T., Jr.; Kraka, E. The pK_a rule in light of local mode force constants. *Chem. Phys. Lett.* **2023**, *826*, 140654.
(84) Peluzo, B. M.; Bodo, F.; Aeindartehran, L.; Runčevski, T.; Kraka, E. Thiabendazole: Fumaric acid as a case study on the salt

cocrystal continuum: A local vibrational mode perspective. *Chem. Phys. Lett.* **2025**, *860*, 141772.
(85) Madushanka, A.; Laird, E.; Clark, C.; Kraka, E. SmartCADD: AI-QM Empowered Drug Discovery Platform with Explainability. *J. Chem. Inf. Model.* **2024**, *64*, 6799−6813.
(86) Madushanka, A.; Moura, R. T., Jr; Kraka, E. QM40, Realistic Quantum Mechanical Dataset for Machine Learning in Molecular Science. *Sci. Data* **2024**, *11* (1), 1376.
(87) Antonio, J. J.; Kraka, E. Metal-ligand bonding and noncovalent interactions of mutated myoglobin proteins: a quantum mechanical study. *Pure Appl. Chem.* **2025**, *97*, 1435−1453.
(88) Freindorf, M.; Kraka, E. Interplay between Metal Ligand Bonds and Hydrogen Bonds in Active Sites of Metal Substituted Myoglobins. *Dalton Trans.* **2025**, *54*, 4096−4111.
(89) Freindorf, M.; Fleming, K.; Kraka, E. Iron-histidine Coordination in Cytochrome b5: A Local Vibrational Mode Study. *ChemPhysChem* **2025**, *26* (7), No. e202401098.
(90) Freindorf, M.; Kraka, E. A Closer Look at the FeS Heme Bonds in *Azatobacter vinelandii Bacterioferritin*: QM/MM and Local Mode Analysis. *J. Comput. Chem.* **2025**, *46* (1), No. e70012.
(91) Kraka, E.; Antonio, J. J.; Freindorf, M. Reaction mechanism − explored with the unified reaction valley approach. *Chem. Commun.* **2023**, *59*, 7151−7290.
(92) Bodo, F.; Erba, A.; Kraka, E.; Moura, R. T., Jr. Chemical Bonding in Uranium-based Materials: A Local Vibrational Mode Case Study of $Cs_2UO_2Cl_4$ and UCl_4 Crystals. *J. Comput. Chem.* **2024**, *45*, 1130−1142.
(93) Peluzo, B. M. T. C.; Moura, R. T., Jr.; Kraka, E. Extraction of uranyl from spent nuclear fuel wastewater via complexation − a local vibrational mode study. *J. Mol. Model* **2024**, *30* (7), 126.
(94) Filatov (gulak), M.; Paolino, M.; Kaliakin, D.; Olivucci, M.; Kraka, E.; Min, S. K. Impact of solvation on the photoisomerisation dynamics of a photon- only rotary molecular motor. *Commun. Phys.* **2024**, *7* (1), 219.
(95) Neto, A. N. C.; Moura, R. T., Jr.; Carlos, L. D.; Malta, O. L.; Sanadar, M.; Melchior, A.; Kraka, E.; Ruggieri, S.; Bettinelli, M.; Piccinelli, F. Dynamics of the Energy Transfer Process in Eu(III) Complexes Containing Polydentate Ligands Based on Pyridine, Quinoline, and Isoquinoline as Chromophoric Antennae. *Inorg. Chem.* **2022**, *61* (41), 16333−16346.
(96) Moura, R. T., Jr; Quintano, M.; Santos-Jr, C. V.; Albuquerque, V. A.; Aguiar, E. C.; Kraka, E.; Carneiro Neto, A. N. Featuring a new computational protocol for the estimation of intensity and overall quantum yield in lanthanide chelates with applications to Eu(III) mercapto-triazole Schiff base ligands. *Opt. Mater.: x* **2022**, *16*, 100216.
(97) Peluzo, B. M. T. C.; Moura, R. T., Jr.; Kraka, E. Conformation and Bonding of Lanthanide(III) Trihalides LnX_3 (Ln = La−Lu; X = F, Cl, Br): A Relativistic Local Vibrational Mode Study. *Inorg. Chem.* **2024**, *63*, 22445−22463.
(98) Machado, F. C.; Quintano, M.; Santos, C. V., Jr.; Neto, A. N. C.; Kraka, E.; Longo, R. L.; Moura, R. T., Jr. Theoretical insights into the vibrational spectra and chemical bonding of Ln(III) complexes with a tripodal N_4O_3 ligand along the lanthanide series. *Phys. Chem. Chem. Phys.* **2025**, *27* (4), 1794−1803.
(99) Saraiva, L. F.; Neto, A. N. C.; Bispo, A. G., Jr.; Quintano, M. M.; Kraka, E.; Carlos, L. D.; Lima, S. A. M.; Pires, A. M.; Moura, R. T., Jr. Role of Vibronic Coupling for the Dynamics of Intersystem Crossing in Eu $^{3+}$++ Complexes: an Avenue for Brighter Compounds. *J. Chem. Theory Comput.* **2025**, *21* (6), 3066−3076.
(100) Kelley, J. D.; Leventhal, J. J. *Problems in Classical and Quantum Mechanics: normal Modes and Coordinates*; Springer, 2017; pp. 95−117.
(101) Barone, V.; Alessandrini, S.; Biczysko, M.; Cheeseman, J. R.; Clary, D. C.; McCoy, A. B.; DiRisio, R. J.; Neese, F.; Melosso, M.; Puzzarini, C. Computational molecular spectroscopy. *Nat. Rev. Methods Primers* **2021**, *1* (1), 37.
(102) Zou, W.; Cremer, D. C_2 in a Box: Determining its Intrinsic Bond Strength for the $X^1\Sigma^+_g$ Ground State. *Chem.−Eur. J.* **2016**, *22* (12), 4087−4099.
(103) Freindorf, M.; Kraka, E.; Cremer, D. A Comprehensive Analysis of Hydrogen Bond Interactions Based on Local Vibrational Modes. *Int. J. Quantum Chem.* **2012**, *112*, 3174−3187.
(104) Verma, N.; Tao, Y.; Kraka, E. Systematic Detection and Characterization of Hydrogen Bonding in Proteins via Local Vibrational Modes. *J. Phys. Chem. B* **2021**, *125*, 2551−2565.
(105) Freindorf, M.; McCutcheon, M.; Beiranvand, N.; Kraka, E. Dihydrogen Bonding−Seen through the Eyes of Vibrational Spectroscopy. *Molecules* **2023**, *28* (1), 263.
(106) Chen, J.; Kato, J.; Harper, J. B.; Shao, Y.; Ho, J. On the Accuracy of QM/MM Models: A Systematic Study of Intramolecular Proton Transfer Reactions of Amino Acids in Water. *J. Phys. Chem. B* **2021**, *125*, 9304−9316.
(107) Holmquist, M. Alpha beta-hydrolase fold enzymes structures, functions and mechanisms. *Curr. Protein Pept. Sci.* **2000**, *1*, 209−235.
(108) Klepeis, J. L.; Lindorff-Larsen, K.; Dror, R. O.; Shaw, D. E. Long-timescale molecular dynamics simulations of protein structure and function. *Curr. Opin. Struct. Biol.* **2009**, *19*, 120−127.
(109) Chodera, J. D.; Swope, W. C.; Pitera, J. W.; Dill, K. A. Long-time protein folding dynamics from short-time molecular dynamics simulations. *Multiscale Model. Simul.* **2006**, *5*, 1214−1226.
(110) Lin, Z.; Akin, H.; Rao, R.; Hie, B.; Zhu, Z.; Lu, W.; Smetanin, N.; Verkuil, R.; Kabeli, O.; Shmueli, Y.; dos Santos Costa, A.; Fazel-Zarandi, M.; Sercu, T.; Candido, S.; Rives, A. Evolutionary-scale prediction of atomic-level protein structure with a language model. *Science* **2023**, *379*, 1123−1130.
(111) Jumper, J.; Evans, R.; Pritzel, A.; Green, T.; Figurnov, M.; Ronneberger, O.; Tunyasuvunakool, K.; Bates, R.; Zidek, A.; Potapenko, A.; Bridgland, A.; Meyer, C.; Kohl, S. A. A.; Ballard, A. J.; Cowie, A.; Romera-Paredes, B.; Nikolov, S.; Jain, R.; Adler, J.; Back, T.; Petersen, S.; Reiman, D.; Clancy, E.; Zielinski, M.; Steinegger, M.; Pacholska, M.; Berghammer, T.; Bodenstein, S.; Silver, D.; Vinyals, O.; Senior, A. W.; Kavukcuoglu, K.; Kohli, P.; Hassabis, D. Highly Accurate Protein Structure Prediction with AlphaFold. *Nature* **2021**, *596*, 583−589.
(112) da Fonseca, A. M.; Caluaco, B. J.; Madureira, J. M. C.; Cabongo, S. Q.; Gaieta, E. M.; Djata, F.; Colares, R. P.; Neto, M. M.; Fernandes, C. F. C.; Marinho, G. S.; dos Santos, H. D. S.; Marinho, E. S. Screening of Potential Inhibitors Targeting the Main Protease Structure of SARS-CoV-2 via Molecular Docking, and Approach with Molecular Dynamics, RMSD, RMSF, H-Bond, SASA and MMGBSA. *Mol. Biotechnol.* **2024**, *66*, 1919−1933.
(113) Shukla, R.; Tripathi, T. *Computer-aided drug design*; Springer, 2020; pp. 133−161.
(114) Vennelakanti, V.; Nazemi, A.; Mehmood, R.; Steeves, A. H.; Kulik, H. J. Harder, better, faster, stronger: Large-scale QM and QM/MM for predictive modeling in enzymes and proteins. *Curr. Opin. Struct. Biol.* **2022**, *72*, 9−17.
(115) Pauling, L. *The nature of the chemical bond and the structure of molecules and crystals: an introduction to modern structural chemistry*; Cornell university press, 1960; Vol. *18*.
(116) Slater, J. C. Directed valence in polyatomic molecules. *Phys. Rev.* **1931**, *37*, 481.
(117) Mulliken, R. S. Overlap integrals and chemical binding1. *J. Am. Chem. Soc.* **1950**, *72*, 4493−4503.
(118) Luo, Y.-R. *Comprehensive handbook of chemical bond energies*; CRC press, 2007.
(119) Badger, R. M. A relation between internuclear distances and bond force constants. *J. Chem. Phys.* **1934**, *2*, 128−131.
(120) Kalescky, R.; Kraka, E.; Cremer, D. Identification of the Strongest Bonds in Chemistry. *J. Phys. Chem. A* **2013**, *117*, 8981−8995.
(121) Quintano, M.; Madushanka, A.; Santos-Jr, C. V.; Machado, F. C.; Kraka, E.; Longo, R. L.; Moura, R. T., Jr Investigating the bimodality of liquid water via chemical bond descriptors and k-means clustering analysis. *J. Mol. Liq.* **2026**, *446*, 129306.
(122) Chan, W. Y.; Wong, M.; Guthrie, J.; Savchenko, A. V.; Yakunin, A. F.; Pai, E. F.; Edwards, E. A. Sequence-and activity-based

screening of microbial genomes for novel dehalogenases. *Microb. Biotechnol.* **2010**, *3*, 107−120.

https://doi.org/10.1021/acs.jpcb.6c02887
J. Phys. Chem. B 2026, 130, 7349−7363